Photoacoustics 41 (2025) 100667

Contents lists available at ScienceDirect

Photoacoustics

journal homepage: www.elsevier.com/locate/pacs

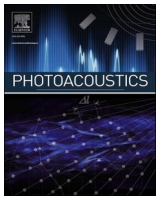

Quantitative pharmacodynamics functional evaluation of Chinese medicine Qizhu formula in mice with dynamic near-infrared photoacoustic imaging

Qing-Juan Wu [a], Lan-Yu Chen [b], Quan-Mei Sun [b], Ning Wang [b], Dong Han [b,**], Wen-Liang Lv [a,*]

[a] Guang 'anmen Hospital, China Academy of Chinese Medical Sciences, Beijing, PR China
[b] Natl Ctr Nanosci & Technol, CAS Ctr Excellence Nanosci, Beijing, PR China

ARTICLE INFO

Keywords:
liver fibrosis
near-infrared photoacoustic imaging
indocyanine green
kinetic parameters
Chinese medicine formula

ABSTRACT

Background & Aims: Effective anti-fibrotic drugs and new non-invasive evaluation methods for liver fibrosis (LF) are urgently needed. Our study aimed to evaluate the histological effects of the Qizhu (QZ) formula on LF and to explore a non-invasive Near-infrared photoacoustic imaging (NIR-PAI) kinetic model for liver function detection and pharmacodynamic evaluation.

Methods: C57BL/6 J mice were randomly divided into six groups (n=6). An LF model was induced by CCl_4 for 8 weeks, followed by an 8-week treatment period. Histological and serological parameters were assessed, and indocyanine green (ICG) metabolism (maximum peak time [T_{max}] and half-life [$T_{1/2}$]) was monitored by NIR-PAI. Spearman correlation analysis was conducted to evaluate correlations.

Results & Conclusions: Histological and serological results confirmed the anti-fibrotic effects of QZ. NIR-PAI kinetic parameters indicated that QZ shortened the T_{max} and $T_{1/2}$ of ICG. There were good correlations between ICG metabolism and liver histopathology. The non-invasive NIR-PAI kinetic model shows potential in liver function detection and pharmacodynamic evaluation.

1. Introduction

Liver fibrosis (LF) is a critical pathological stage in the progression of chronic liver disease to cirrhosis and hepatocellular carcinoma (HCC). The main histological signs of LF include necrosis of hepatocytes and aberrant extracellular matrix (ECM) deposition [1,2]. Currently, there is no effective treatment for LF other than liver transplantation. Its serious complications pose a significant threat to patient health, resulting in high morbidity and mortality rates. There is an urgent need for effective anti-fibrotic drugs [3].

At present, LF clinical treatments mainly focus on anti-etiology, including antivirals, immunosuppression, alcohol withdrawal, and others. Traditional Chinese medicine (TCM) has demonstrated notable benefits in reducing patients' clinical symptoms and regulating multiple pharmacological targets [4]. Qizhu formula (QZ) is a Chinese medicine formula derived from TCM theory and clinical application experience. It is composed of 10 natural Chinese herbs, with the main active ingredients including Astragalus (Astmgali Radix), Curcuma phaeocaulis Val (Curcumae Rhizoma), Salvia miltiorrhiza Bge (Salviae Miltiorrhizae), and Atractylodes macrocephala Koidz (Macrocephalae Rhizoma). Studies have reported the therapeutic effects of these ingredients in fibrotic diseases [5–8]. In the early stage, we clinically demonstrated that QZ has a definite effect and safety in 134 LF patients. Results showed that QZ could effectively improve patients' clinical symptoms such as hepatalgia and fatigue, and decrease abnormal liver indicators such as aminotransferases and bilirubin [9]. However, liver biopsy, an invasive examination with potential complications, is not well accepted in clinical practice. This brings challenges in obtaining reliable histopathological data to evaluate the efficacy of QZ. Effective anti-fibrotic drugs and new non-invasive evaluation methods are urgently needed.

Recently, the rapid development of imaging techniques, featuring advantages of being non-invasive, simple, and compliant, includes

Abbreviations: ALD, alcoholic liver disease; ALT, alanine aminotransferase; AST, aspartate aminotransferase; CD31, cluster of differentiation 31; Col-I, type I collagen protein; Col-IV, type IV collagen protein; ECM, extracellular matrix; HA, hyaluronic acid; ICG, indocyanine green; LF, liver fibrosis; LN, laminin; MMP-2, matrix metalloproteinase-2; NIR-PAI, Near-infrared photoacoustic imaging; PA, photoacoustic; PACT, photoacoustic computed tomography; PCIII, type III procollagen; QZ, Qizhu formula.

* Correspondence to: Guang 'anmen Hospital, No.5 Beixiange, Xicheng District, Beijing 100053, PR China.
** Correspondence to: Natl Ctr Nanosci & Technol, CAS Ctr Excellence Nanosci, Beijing 100190, PR China.
E-mail addresses: dhan@nanoctr.cn (D. Han), 1733463497@qq.com (W.-L. Lv).

https://doi.org/10.1016/j.pacs.2024.100667
Received 12 August 2024; Received in revised form 9 November 2024; Accepted 10 November 2024
Available online 14 November 2024

ultrasonography (US), transient elastography (TE), magnetic resonance elastography (MRE), and computed tomography (CT). These imaging techniques supplement the limitations of histopathological detection [10–12]. However, imaging results are easily affected by liver inflammation, intrahepatic conditions, and hepatic amyloidosis, etc., which result in insufficient accuracy [13–15]. Near-infrared photoacoustic imaging (NIR-PAI) is a novel non-invasive imaging method with high spatial resolution and deep penetration depth (700–1700 nm). NIR-PAI, with its high contrast, enables faster, safer, easier, more precise, and less expensive clinical testing than positron emission tomography or computed tomography. Preclinical studies have reported its potential as a diagnostic and image-guiding tool [16,17]. Indocyanine green (ICG) is an agent approved by the US Food and Drug Administration (FDA) for clinical use [18], and the ICGR15 (15-minute retention rate of ICG) test has been carried out worldwide to evaluate liver reserve function and reflect the amount of functional liver cells in surgical operations. Coincidentally, ICG exhibits PAI properties, with an absorption peak of approximately 800 nm. In recent years, preclinical experiments on dynamic liver function assessment using ICG combined with PAI have been conducted [19,20]. Preliminary findings suggest that the combination of PAI and ICG offers non-invasive, quantitative, and dynamic advantages. More importantly, there is a statistically significant correlation with histopathological content, indicating that this combination may provide a reliable quantitative model for the diagnosis and pharmacodynamic evaluation of liver fibrosis.

Our study established a liver fibrosis mouse model and treated it with the QZ formula. Histological and serological assessments, as well as NIR-PAI kinetic parameters of ICG, including the maximum peak time (T_{max}) and half-life ($T_{1/2}$), were employed to evaluate the anti-liver fibrosis efficacy of QZ. Obtaining histological confirmation of QZ's efficacy against liver fibrosis could expedite its clinical adoption. The non-invasive NIR-PAI kinetic model correlates with histological and serological markers, thus establishing a dependable, quantitative, and non-invasive approach for clinical liver function assessment and pharmacodynamic analysis.

2. Materials and methods

2.1. Animal models and drugs intervention

Male C57BL/6 J mice, aged 4–6 weeks, were used in this study. The protocol was approved by the ethics committee of the National Center for Nanoscience and Technology. Mice were randomly and evenly divided into six groups (n=6): healthy group (Control), fibrosis model group (Model), silybin treatment group (Positive), and Qizhu formula groups with high, medium, and low doses (QZ-L, QZ-M, QZ-H). Model mice were injected intraperitoneally with 5 μl/g body weight (bw) of a 10 % (vol/vol) CCl_4 solution (MacLean, C805332) twice a week for 8 consecutive weeks. Drug intervention began in the third week of CCl_4 injections. The gavage dose of silybin was 31.5 mg/kg bw/day, and the three Qizhu formula doses were 1.35 g/kg bw/day, 2.7 g/kg bw/day, and 5.4 g/kg bw/day. The control and model groups were gavaged with the same volume of 0.9 % physiological saline. The administration frequency was once a day for 8 weeks.

2.2. Ultrasound grayscale imaging of the liver

A small animal ultrasound machine (Vevo, VisualSonics Vevo LAB) was used to detect the ultrasound grayscale imaging of the liver. Mice were fasted with water for 6 hours before the experiment and anesthetized by inhalation of 2 % isoflurane. Their feet were gently fixed, the hair on the abdomen was removed with depilatory cream to fully expose the liver area, and conductive gel was applied to the exposed skin. The mice were then connected to the physiological signal acquisition unit and scanned using B-Mode grayscale imaging. Fiji: ImageJ software was used to measure the grayscale values and hepatic portal vein diameters of the liver. Histograms of grayscale images were generated using the OpenCV cv2.calcHist function in the Python module. The selection criterion for the region of interest (ROI) was to identify sections of liver tissue free from major blood vessels and hepatic lobules. The specified size of the ROI was calibrated to enable random positioning throughout all hepatic tissue areas, avoiding large vessels and lobules in each liver section. We modified the quantitative method of ultrasound grayscale value based on the approach described in the literature. By comparing the ultrasound grayscale signals from the livers of mice in each group with those from normal mice, we obtained the ultrasound gray scale ratio (UGSR) [21,22].

2.3. Three-dimensional (3D) Photoacoustic (PA) imaging of the mouse liver

The mouse liver was imaged using a PAI system (Nexus 128, Endra Inc.) at 800 nm, which corresponds to the absorption peak of ICG in blood. The hair on the mice's abdomen was removed to expose the liver area, and then the mice were anesthetized using 2 % isoflurane. The anesthetized mice were fixed on the animal tray within the Nexus scanning bin, and scanning parameters were set. The scanning duration was 1.2 minutes, with the mode set to "step and shoot." The number of angles was set to 36, and the number of pulses per angle to 20. Before ICG injection, the first scan was performed and recorded as the 0-second imaging. Subsequently, ICG was injected via the tail vein at a dose of 3 μmol/kg·bw, and the second scan was performed 90 seconds after the injection, followed by scans at 200, 300, and 600 seconds. The scanning data were imported into custom-written MATLAB (R2014a) for 3D imaging analysis, and the statistical analysis of photoacoustic intensity was performed using Fiji: ImageJ software.

2.4. Plotting of PA liver function curve

We selected the region of interest in each mouse liver PA images and measured the PA signal intensity (SI) values to plot the PA liver function curve. Relative enhancement (RE) was calculated using Eq.(a)[20].

$$RE(T) = \frac{SI_{(T)} - SI_{(T_0)}}{SI_{(T_0)}} * 100\% \quad (a)$$

Where the SI(T) is the liver PA signal intensity after ICG injection, the SI (T_0) is the average contrast signal intensity before injection. The time course of RE was plotted to identify the liver PA liver function curve. The absorption rate and excretion rate of PA were calculated by the fitted curve equations using an empiric mathematic model(b)[23].

$$RE(T) = \begin{cases} 0 & 0 \le T < T_0 \\ A \bullet \left[1 - e^{-\alpha(T)-(T_0)}\right] q\, e^{-\beta(T)-(T_0)} & T_0 \le T \end{cases} \quad (b)$$

Where A is the upper limit of the RE, α is the rate of contrast uptake(s^{-1}), β is the rate of contrast washout(s^{-1}), q is a parameter related to the slope of the early uptake, and T_0 is the rise time point (s). The T_{max} RE and $T_{1/2}$ of the elimination RE were calculated from the fitted curve.

2.5. Liver pathological staining

Freshly isolated liver tissues were fixed in 4 % paraformaldehyde (vol/vol) for more than 24 hours, embedded in paraffin, and sectioned by conventional methods for histopathological examination. The histopathological sections were stained with hematoxylin and eosin (HE), Sirius Red, and immunofluorescence. Pathological changes were observed and photographed for analysis. Antibodies against matrix metalloproteinase-2 (MMP-2), type I collagen protein (Col-I), and cluster of differentiation 31 (CD31) were purchased from Sigma-Aldrich. Fiji: ImageJ software was used to measure the areas positive for Sirius

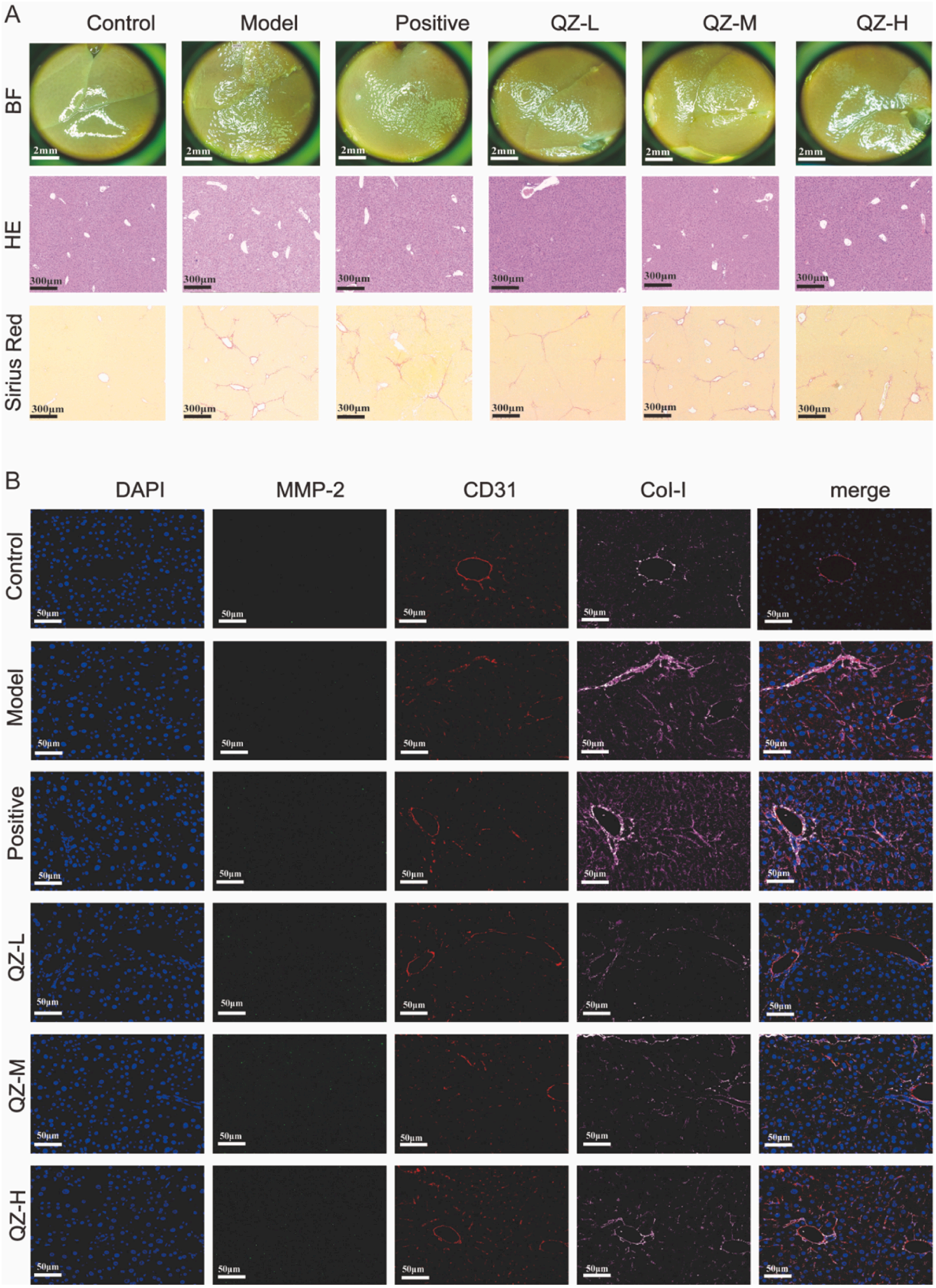

Fig. 1. Histopathologic analysis of mouse liver at different intervention of modeling. A, Photographs of mouse liver (BF), scan bar = 2 mm. Photomicrographs obtained with hematoxylin-eosin staining (HE) and Sirius red staining, scan bar = 300μm. B, Immunofluorescence staining of liver tissue with DAPI/nucleus (blue), MMP-2(green), CD31 (red), Col-I (pink) and merge, respectively. Scan bar = 50μm.

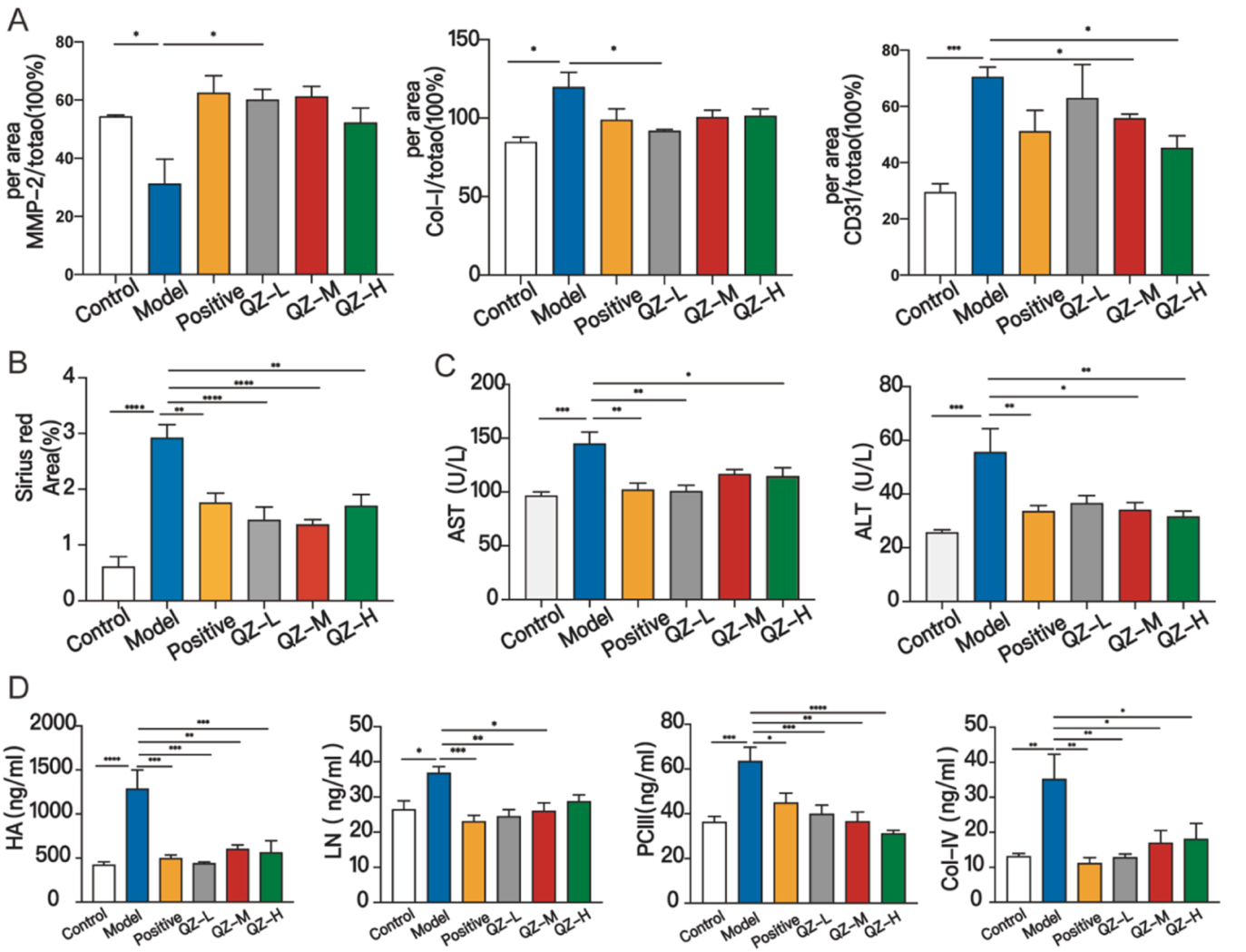

Fig. 2. Statistical analysis of the histopathologic staining positive area and liver function parameters serology content in different intervention of modeling mouse. A, the percentages of positive areas for immunofluorescence staining for MMP-2, CD31 and Col-I in liver tissue. B, the percentages of positive areas for Sirius red in liver tissue. C, The ALT and AST contents in the serum of different intervention of modeling mouse. D, the HA, LN, Col-IV and PCIII contents in the serum of different intervention of modeling mouse. *$P<0.01$, **$P<0.005$, ***$P<0.001$, ****$P<0.0001$.

Red, MMP-2, Col-I, and CD31 immunohistochemical staining.

2.6. Serology contents detection

After the mice were anesthetized, approximately 1–1.5 ml of blood was collected from each mouse and left to stand for 2 hours at room temperature before being centrifuged for 15 minutes at 3000 rpm. The upper serum layer was carefully aspirated and stored at −80°C for serology content detection. Before serology content detection, the serum samples were thawed and centrifuged again. The automatic biochemical analyzer (Chemray 240, Shenzhen Life Technology Co., LTD) was set to the corresponding parameters for automatic determination.

2.7. Statistical analysis

Data are presented as mean±SD. GraphPad Prism (version 8.0) software was used for statistical analysis. Data were analyzed using ANOVA for Gaussian distribution and the Kruskal-Wallis test for non-Gaussian distribution. When performing correlation analysis, a normal distribution test was conducted on continuous variable data from different groups. Spearman's rank correlation was used to evaluate the relationship between PAI results and liver histologic scores and liver function serology contents. $P < 0.05$ was considered statistically significant.

3. Results

3.1. Liver histopathologic analysis

Histology is the "gold standard" for evaluating liver fibrosis. In this study, HE staining, Sirius Red staining, and immunofluorescence staining were used to assess the histological features. In the normal group (control), the liver under bright field (BF) view displayed a soft texture, smooth surface, and light, glossy color; HE staining revealed normal morphology of hepatic sinusoids and hepatocytes; and Sirius Red staining showed no significant red collagen fiber deposition. However, in the fibrotic group (model), the BF view of the liver appeared rough in texture, with a grainy surface, dull color, and less luster; HE staining revealed disorder in hepatic cords, necrosis of hepatocytes, nucleopyknosis, and formation of inflammatory cells; Sirius Red staining revealed extensive collagen fiber deposition between hepatic lobules. Conversely, in the four treatment groups (positive, QZ-L, QZ-M, QZ-H), the BF view, HE staining, and Sirius Red staining all showed improvements in hepatocyte damage and collagen fiber deposition (Fig. 1A), suggesting the

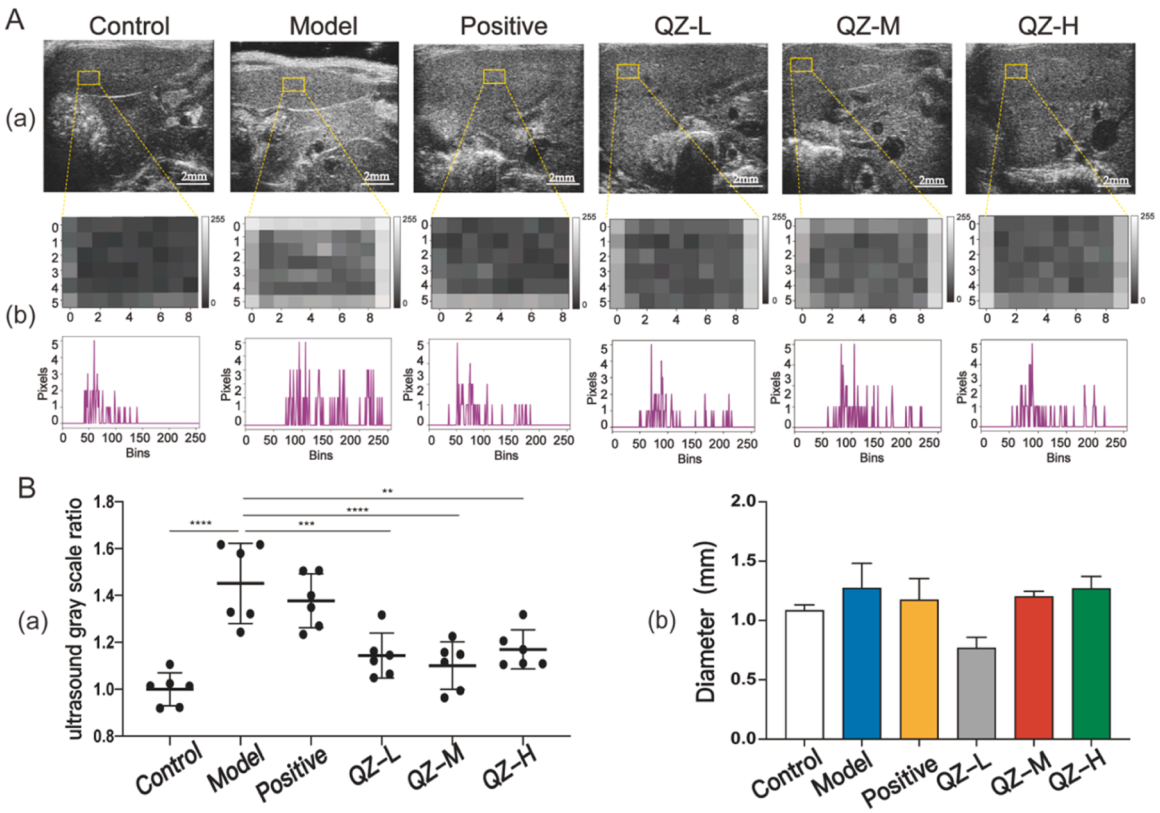

Fig. 3. US images of mouse liver at different intervention of modeling without use of an exogenous contrast agent. A(a), The US grayscale images of mice liver in live mice, ROI area is 1.306*0.822 mm. A(b), The grayscale histogram of different intervention modeling. B(a), Statistical analysis of the US gray scale ratio (UGSR) in different intervention of modeling. B(b), Statistical analysis of the diameters of hepatic portal vein in different intervention modeling. *P<0.01, **P<0.005, ***P<0.001, ****P<0.0001, specific P values are in Table1.

histological effects and hepatocyte protective efficacy of the Qizhu formula.

During the progression of LF, increased Col-I and decreased MMP-2 are the main factors in ECM accumulation [24,25]. Immunofluorescence staining results showed that MMP-2 decreased while Col-I increased in the model group; in contrast, in the four treatment groups, the expression of MMP-2 showed an increasing trend, while Col-I significantly decreased (Fig. 1B). The expression of CD31 increases with the progression of liver fibrosis; an increase in CD31 indicates the capillarization of liver sinusoids. The results of CD31 immunofluorescence staining increased in the model group but decreased in the treatment groups, suggesting that the pathological manifestations of capillarization were improved in the treatment groups compared with the model group (Fig. 1B). The immunofluorescence staining results further confirmed the histological effects of Qizhu on anti-fibrotic activity.

3.2. *Quantitative statistical analysis of liver function parameters in tissue staining and serology content*

Aimed at the quantitative evaluation of the anti-hepatic fibrosis efficacy of QZ, we statistically analyzed the staining positive areas to obtain objective evidence. Results showed that Col-I (control, 84.79 % ±4.47; model, 119.78 %±16.40; positive, 98.90 %±12.09; QZ-L, 91.88 %±1.67; QZ-M, 91.88 %±1.67; QZ-H, 101.49 %±7.80) and CD31 (control, 29.54 %±2.97; model, 70.48 %±3.48; positive, 51.15 % ±7.44; QZ-L, 62.92 %±12.00; QZ-M, 55.77 %±1.47; QZ-H, 45.23 % ±4.29) were significantly increased in the model group compared to the control group, while they were decreased in the four treatment groups compared to the model group. MMP-2 (control, 54.38 %±4.85; model, 31.28 %±8.41; positive, 62.51 %±5.83; QZ-L, 60.14 %±3.52; QZ-M, 61.22 %±3.46; QZ-H, 52.22 %±5.06) was significantly decreased in the model group compared to the control group, while it increased in the four treatment groups compared to the model group (Fig. 2A). Sirius Red staining results showed that, in the model group, the collagen fiber deposition was significantly more pronounced than in the control group, and the deposition area significantly decreased in the four treatment groups compared to the model group (Fig. 2B, control, 0.61 %±0.4; model, 2.92 %±0.66; positive, 1.75 %±0.45; QZ-L, 1.44 %±0.65; QZ-M, 1.37 %±0.24; QZ-H, 1.70 %±0.51). The statistical analysis results provide reliable quantitative evidence of the anti-fibrotic effects of QZ granules, suggesting that the QZ formula could reverse the abnormal deposition of ECM, especially decreasing the expression of collagen fibers stained with Sirius Red.

We further detected the serological contents commonly used to evaluate liver fibrosis in clinical settings. AST and ALT are the most frequently used clinical parameters in the prediction and evaluation of liver fibrosis [26,27]. Statistical results showed that AST (control, 96.66 IU/L±8.44; model, 145 IU/L±23.98; positive, 102.2 IU/L±13.4; QZ-L, 100.8 IU/L±12.21; QZ-M, 116.6 IU/L±9.83; QZ-H, 114.4 IU/L ±18.33) and ALT (control, 25.67 IU/L±2.42; model, 55.6 IU/L±19.59; positive, 33.6 IU/L±4.67; QZ-L, 36.6 IU/L±6.27; QZ-M, 34 IU/L±6.16; QZ-H, 31.6 IU/L±4.61) were significantly increased in the model group compared to the control group, while they decreased in the four treatment groups (Fig. 5C). Hyaluronic acid (HA) and laminin (LN), along with type IV collagen (Col-IV) and type III collagen (PCIII), are the main components of ECM. Therefore, the levels of LN, HA, Col-IV, and PCIII in serum are used to evaluate liver fibrosis. Serological statistics results showed that LN (control, 26.44 ng/ml±6.04; model, 36.79 ng/ml ±4.00; positive, 23.04 ng/ml±4.25; QZ-L, 24.47 ng/ml±4.34; QZ-M, 26.00 ng/ml±5.14; QZ-H, 28.71 ng/ml±4.13), HA (control, 422.63 ng/ml±86.19; model, 1285.21 ng/ml±479.66; positive,

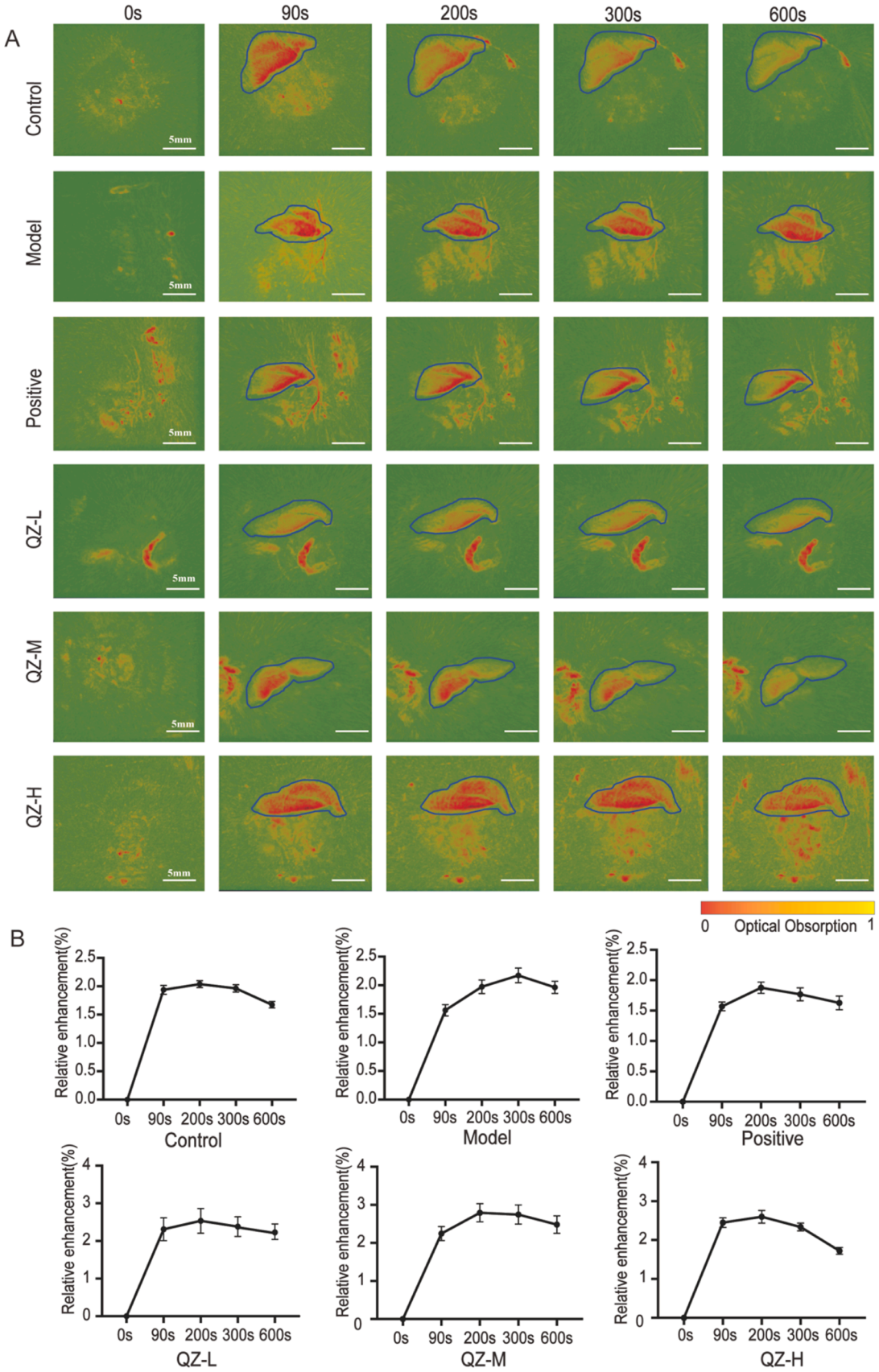

Fig. 4. Time course of dynamic near-infrared photoacoustic imaging of mouse liver. A, Dynamic contrast-enhanced PA imaging for different groups before (0 s) and after indocyanine green injection (90s-600s), the blue line area is liver. B, PA liver function curves. (Figure displayed the 2D pictures of the cross-section of 3D liver PA imaging, the statistics of PA signals are the 3D quantitative results.).

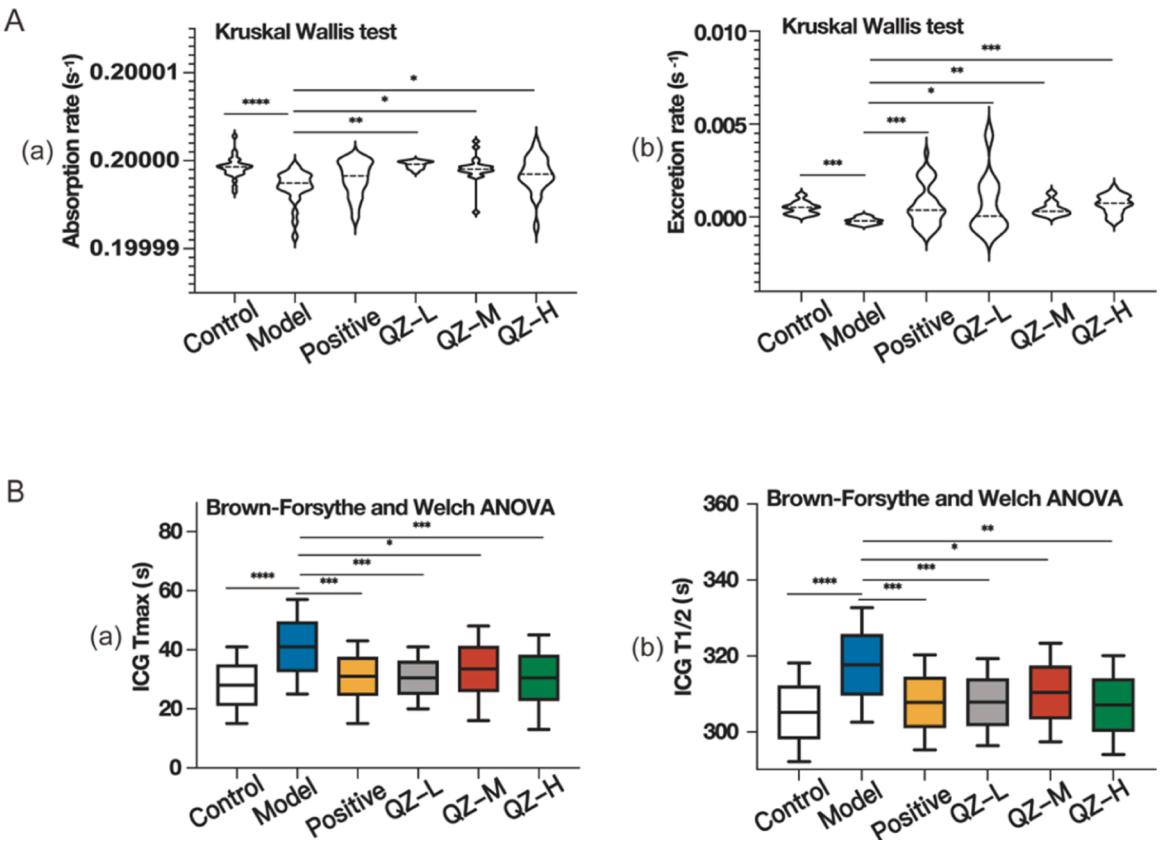

Fig. 5. Time Course and kinetic parameters of PAI of Mouse Liver. A, Rates of indocyanine green (ICG) absorption and excretion. B, The ICG metabolic parameters of maximum peak time (T_{max}) and half-life ($T_{1/2}$) in mouse livers.

498.60 ng/ml±82.50; QZ-L, 440.10 ng/ml±37.11; QZ-M, 601.44 ng/ml ±108.39; QZ-H, 562.41 ng/ml±301), Col-IV (control, 13.12 ng/ml ±2.02; model, 35.20 ng/ml±15.83; positive, 11.16 ng/ml±3.55; QZ-L, 12.78 ng/ml±2.23; QZ-M, 16.94 ng/ml±8.01; QZ-H, 18.09 ng/ml ±9.88), and PCIII (control, 36.25 ng/ml±6.26; model, 63.48 ng/ml ±13.94; positive, 44.92 ng/ml±9.67; QZ-L, 39.93 ng/ml±8.68; QZ-M, 36.53 ng/ml±9.51; QZ-H, 31.15 ng/ml±3.23) levels in the model group were significantly higher than those in the control group, while they were significantly decreased in the four treatment groups (Fig. 5D). The above serological parameters were consistent with the trend of clinical parameters, and statistical analysis results suggested the therapeutic effects of the positive drug (silybin) and QZ formula drugs. Although there was no significant statistical difference among the four treatment groups, the three QZ groups generally showed an advantage over the positive group. In addition, the three dose groups of QZ granules showed a dose-response relationship in some individual parameters (AST, LN, PC-III, Col-IV).

3.3. US imaging and three-dimensional (3D) NIR-PAI of liver

We have demonstrated the anti-fibrotic effects of the drugs histologically and serologically. Subsequently, we assessed liver function in LF mice using both conventional US and NIR-PAI methods. Ultrasound grayscale imaging was performed on the coronal plane of the mouse liver without an exogenous contrast agent. In the control group, the liver edge appeared smooth, with uniform parenchyma and moderate ultrasound intensity. Conversely, in the model group, dullness was observed in the liver parenchyma, along with hepatic portal vein dilatation and nodular changes, leading to increased ultrasound intensity (Fig. 3A(a)). By drawing the gray histogram of liver US imaging, it can be seen that the number of high-intensity gray pixels increased in the model group but decreased in the four treatment groups (Fig. 3A(b)). US grayscale ratio (UGSR) statistics showed a significant increase in the model group compared to the control group (Fig. 3B(a), control: 1.0±0.25; model: 1.45±0.17). In the four treatment groups, the UGSRs decreased versus the model group, and the three QZ groups showed a more pronounced reduction than the positive group, with the difference being statistically significant (Fig. 3B(a), positive: 1.37±0.11; QZ-L: 1.14±0.09; QZ-M: 1.10±0.10; QZ-H: 1.17±0.08). Additionally, the hepatic portal vein diameter increased in the four treatment groups (Fig. 3B(b)). These results are consistent with clinical ultrasonography images of liver fibrosis patients and treated patients.

Next, we employed the NIR-PAI kinetic model to assess liver function by recording ICG metabolism. Fig. 4 shows the dynamic NIR-PAI results of mouse livers in different groups at 800 nm. PAI revealed a decreased capacity of the model group to absorb and expel ICG compared to the control group, while the liver's ability to metabolize ICG increased in all four treatment groups. We conducted 3D imaging of mouse livers in each group (Fig. 4A) and outlined the PA liver function curve (Fig. 4B). Fig. 4 displays the 2D pictures of the cross-section of 3D liver PA imaging, and the statistics of PA signals are the 3D quantitative results.

3.4. Statistical analysis of NIR-PAI kinetic parameters

In order to quantitatively analyze the NIR-PAI parameters, we performed curve fitting on the liver function curve using an empirical mathematical model and calculated the absorption and excretion rates of ICG. We took the maximum absorption time [T_{max}] and half-life time [$T_{1/2}$] of ICG as the quantitative parameters of the NIR-PAI kinetic model. The absorption rate and excretion rate of PA were determined by fitting curve equations. Results showed that the absorption rate and excretion rate decreased in the model group but increased in the four treatment groups (Fig. 5A). We calculated T_{max} and $T_{1/2}$ of ICG for each group according to the fitting Eq. (b). The results showed that T_{max} (sec)

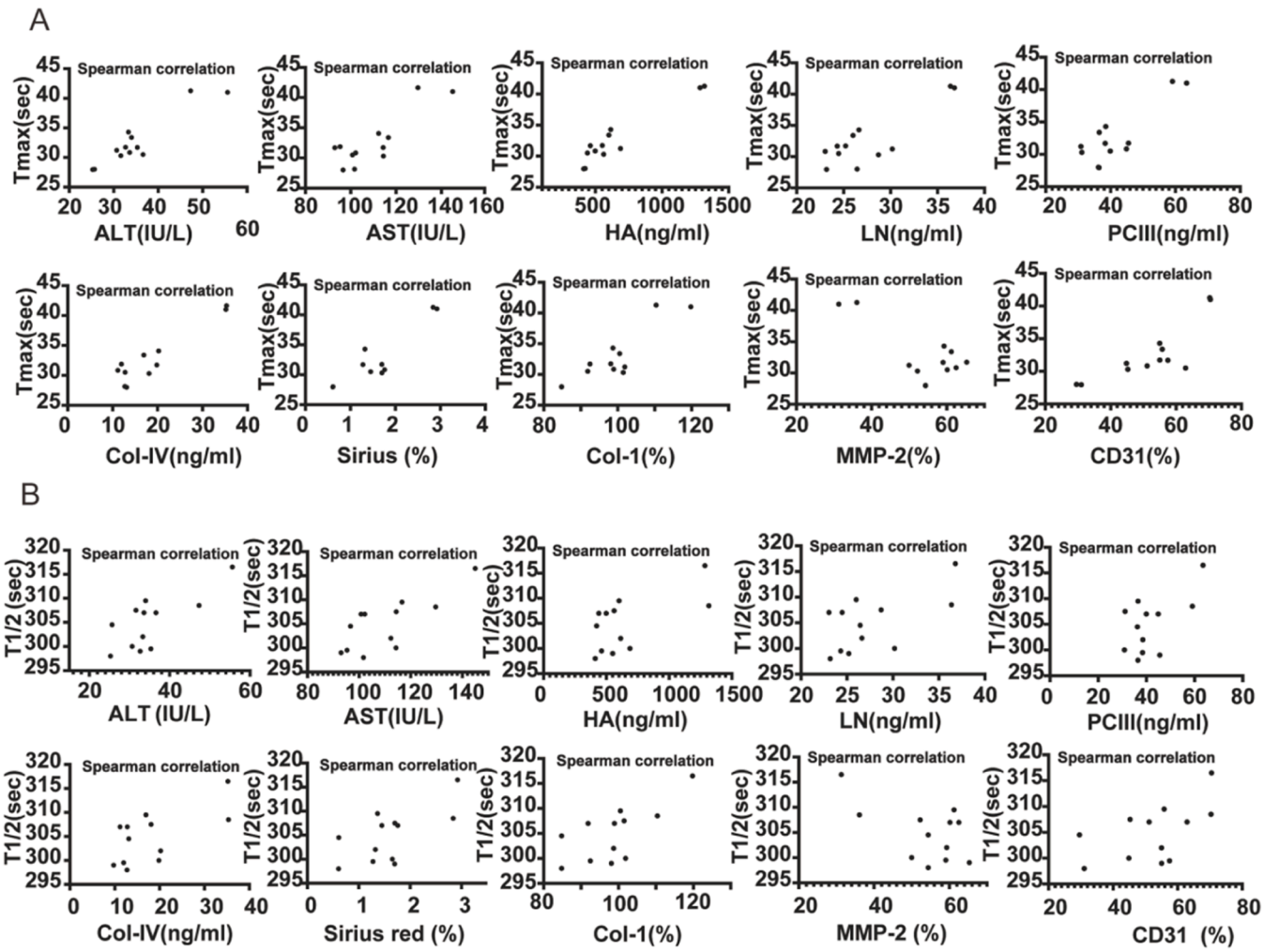

Fig. 6. Spearman correlations between the kinetic parameters for dynamic contrast-enhanced photoacoustic imaging with ICG and the histopathologic & serologylogic score in each group. A, Correlation between the maximum peak time (T_{max}) and the Sirius red–positive area, the Col-I–positive area, the MMP-2–positive area, the CD31–positive area, and the ALT and AST content. B, Correlation between the half-life ($T_{1/2}$) and Sirius red–positive area, the Col-I–positive area, the MMP-2–positive area, the CD31–positive area, and the ALT and AST content.

(Fig. 5B(a), T_{max} (mean±SD): control, 28 s±7.93; model, 41 s±9.67; positive, 30.84 s±7.67; QZ-L, 30.5 s±6.49; QZ-M, 33.4 s±8.99; QZ-H, 30.3 s±9.14; $P<0.05$) and $T_{1/2}$ (sec) (Fig. 5B(b), $T_{1/2}$ (mean±SD): control, 304.5 s±7.65; model, 316.5 s±8.80; positive, 307 s±7.36; QZ-L, 309.5 s±6.78; QZ-M, 309.5 s±7.65; QZ-H, 307.5 s±7.65; $P<0.05$) were significantly extended in the model group. Conversely, they were shortened across the treatment groups, with no statistical difference among the four treatment groups. The T_{max} and $T_{1/2}$ of ICG provided a NIR-PAI kinetic parameter model for evaluating liver metabolic function over time and space.

3.5. Correlation analysis between NIR-PAI kinetics model and histopathology and serology contents

Lastly, we evaluated the relationship between NIR-PAI kinetic parameters and histopathological positive area with serological contents. As shown in Fig. 6A, there was a positive correlation between the dynamic parameters of ICG T_{max} and the histopathological positive area and serological contents. The Spearman's ρ values for histopathological positive area versus T_{max} were: Sirius Red staining, 0.753 (95 % CI: 0.261, 0.935); Col-I, 0.670 (95 % CI: 0.136, 0.902); CD31, 0.748 (95 % CI: 0.288, 0.928); MMP-2, −0.136 (95 % CI: −0.669, 0.489), respectively. The Spearman's ρ values for serological contents versus T_{max} were: AST, 0.565 (95 % CI: 0.0016, 0.8559); ALT, 0.713 (95 % CI: 0.217, 0.917); PCIII, 0.6507 (95 % CI: 0.103, 0.895); LN, 0.532 (95 % CI: −0.080, 0.852); HA, 0.832 (95 % CI: 0.479, 0.953); Col-IV, 0.627 (95 % CI: 0.023, 0.896), respectively. Fig. 6B shows the positive correlation between the dynamic parameters of ICG $T_{1/2}$ and the histopathological positive area and serological contents. The Spearman's ρ values for histopathological positive area versus $T_{1/2}$ were: Sirius Red staining, 0.624 (95 % CI: 0.058, 0.886); Col-I, 0.6561 (95 % CI: 0.1129, 0.8974); CD31, 0.5219 (95 % CI: −0.0934, 0.8487); MMP-2, −0.305 (95 % CI: −0.7565, 0.3429), respectively. The Spearman's ρ values for serological contents versus $T_{1/2}$ were: AST, 0.778 (95 % CI: 0.351, 0.937); ALT, 0.634 (95 % CI: 0.07526, 0.8897); PCIII, 0.326 (95 % CI: −0.323, 0.767); LN, 0.522 (95 % CI: −0.0934, 0.8487); HA, 0.545 (95 % CI: −0.0593, 0.858); Col-IV, 0.5849 (95 % CI: −0.002697, 0.8723), respectively. Correlation analysis showed that the kinetic parameters of T_{max} and $T_{1/2}$ were highly correlated with the results of liver histopathology (Sirius Red staining, Col-I, Col-IV) and serology (AST, ALT). The results suggest that ICG metabolism is associated with liver fibrosis status, which suggests that PAI can be used to evaluate liver function and serve as a dynamic parameter for drug efficacy evaluation.

4. Discussion

Liver fibrosis is the result of chronic liver injury and frequently progresses to cirrhosis, liver failure, portal hypertension, and

hepatocellular carcinoma (HCC). It is crucial to shorten the continuous progression to reduce the serious adverse consequences of chronic liver diseases [28].

Currently, there are no reliable medications to treat liver fibrosis [29]. Current research on anti-liver fibrosis is focusing on the regulation of molecular targets, with most still in phase II and phase III clinical trials. Natural substances, immunology, and genetic approaches have demonstrated considerable advantages in anti-fibrotic therapies [30, 31]. TCM formulas, as primary natural medicine practitioners derived from clinical experience, have shown anti-liver fibrosis effects clinically, such as reducing collagen fiber deposition and the incidence of cirrhosis. TCM has drawn attention to its benefits in treating LF due to multi-target regulation, improved clinical symptoms, and fewer side effects. However, the multi-target regulation characteristic of TCM means its complex mechanisms cannot be adequately explained by common methodologies, significantly limiting its further promotion and international application.

Another major obstacle to the advancement of anti-fibrotic medications is the absence of reliable quantitative tools for assessing LF [31, 32]. The "gold standard" for LF diagnosis is liver biopsy, which is not commonly accepted in clinical practice due to its well-known limitations (invasiveness, uncommon but serious complications, and sampling inconsistency). Considerable work has been done to develop simple and non-invasive tools that can be easily used in routine clinical practice and drug development [33]. ICG can rapidly bind to hemoglobin and is only absorbed by the liver; during liver fibrosis, the metabolism of ICG is hindered by abnormal deposition of the ECM and hepatocyte necrosis, making ICG an ideal contrast agent for liver function evaluation [34]. With the development of imaging detection, PAI has been previously reported for monitoring ICG-based agent dynamic absorption and clearance in tumor tissues [35], and the combination of PAI with ICG is emerging as a potentially non-invasive method in clinical practice.

In our study, we assessed the histological efficacy of the QZ formula in mice as an alternative to the limited clinical liver biopsy. We also evaluated the serological markers of liver fibrosis. At the same time, silybin, as the most commonly used liver-protective drug, was identified as effective in anti-fibrotic activity in our previous study [36], hence silybin was chosen as the positive control drug. Clinical liver biopsies usually involve collagen fiber staining, and by analyzing the collagen fiber positive area, the severity of LF can be identified. Our study utilized Sirius Red staining and immunofluorescence staining to label collagen fibers and Col-I, respectively, demonstrating that the QZ formula can effectively reduce the abnormal deposition of the ECM ($P<0.05$). Additionally, serological results indicated a reduction in transaminase levels and expression of LF molecules with QZ treatment, consistent with clinical trial results.

Next, we explored the non-invasive method of the PAI system combined with ICG to evaluate the LF status in mice. Previously, ICG-based probes combined with PAI were used in HCC lesion detection, and dynamic contrast-enhanced PAI was used to plot the ICG curve in liver fibrosis mice [20]. Recently, preclinical studies used the PAI system with ICG to evaluate the relationship between liver reserve function and liver fibrosis in a rabbit model, and the results showed that ICG clearance was significantly reduced in the model group, suggesting an impairment of liver reserve function [37]. Consistent with previous findings, our results showed that ICG excretion in the 8-week LF model decreased to more than 300 seconds, and the ICG absorption rate and excretion rate were both significantly increased compared to the healthy liver. This demonstrates the robustness of the NIR-PAI with ICG resolution model in distinguishing fibrotic and normal liver tissue. However, the photoacoustic data acquisition frequency was constrained by the capabilities of the employed machine model. To substantiate the validity and reliability of our findings, we correlated our results with literature data, revealing that the ICG metabolic curve derived from photoacoustic signals in this study was roughly the same as those reported for mice with LF [20]. Furthermore, we integrated photoacoustic computed tomography (PACT) with the signal fitting method, demonstrating its applicability in chronic alcoholic liver disease (ALD) and hereditary tyrosinemia type I (HT1) models for assessing liver reserve and renal metabolic functions. The outcomes consistently validated the accuracy of PAI in measuring liver function. PAI's non-invasive nature and high-contrast resolution offer distinct advantages over conventional clinical imaging, holding the potential to significantly augment the comprehensive evaluation of hepatic and renal pathologies [38–40].

On the basis of proving that NIR-PAI is a reliable diagnostic tool, we further used NIR-PAI with ICG to evaluate the efficacy of anti-liver fibrosis drugs. Results showed that the NIR-PAI kinetic parameters of ICG (T_{max} and $T_{1/2}$) in the four drug treatment groups were lower than those in the model group and were positively correlated with histopathological (Sirius Red staining, Col-I) and serological (ALT, AST, Col-IV) contents ($P < 0.05$). At the same time, the three QZ groups showed an advantage over the positive group, and the three dose groups of QZ granules showed a trend of dose-response relationship in some individual parameters. Although there was no significant statistical difference in drug optimal efficiency and dose-response relationship, those liver function parameters were consistent with previous studies [36]. In this study, the evaluation of liver reserve function in fibrotic mice treated with three dosages of QZ revealed that the high-dose group performed better in shortening the maximum peak absorption time (T_{max}) of ICG and reducing its half-life ($T_{1/2}$). Additionally, when integrated with liver photoacoustic imaging results (Fig. 4), the QZ high-dose group outperformed the low and medium dosage groups in enhancing liver reserve function. This phenomenon suggests the possibility of NIR-PAI as an evaluation tool for drug efficacy. However, the high-dose group of QZ did not consistently show superiority in reducing extracellular matrix deposition and serum fibrosis biomarkers compared to the low and medium dosage groups (Fig. 2). This indicates the complex mechanism of QZ as a type of TCM formula. To maximize clinical benefits, a comprehensive evaluation of drug efficacy considering multiple liver function indicators is necessary. To optimize clinical outcomes, a comprehensive evaluation of drug efficacy—taking into account multiple indicators of liver function—is essential. In this context, non-invasive and easy-to-use methods (such as NIR-PAI) can assist clinicians in making more comprehensive judgments on drug efficacy, thereby facilitating the clinical application of more effective anti-fibrotic drugs.

There are still limitations to our study. Firstly, the penetration depth of NIR is insufficient; the first NIR region (NIR-I, 700–900 nm) can penetrate only 2–3 cm, and the second near-infrared region (NIR-II, 1000–1700 nm) up to 5–6 cm, which limits its clinical application. Worthy of expectation, there has been recent research aimed at developing new ICG-sized tunable contrast agents for targeted NIR-PAI, suggesting potential for clinical development [19]. Secondly, the liver fibrosis mouse model induced by CCl_4 injection does not reflect the clinical onset mechanism of LF, which may introduce potential bias into our study results. Lastly, due to constraints in NIR imaging instruments, the description and imaging time in our study remain long. NIR-PAI systems with higher resolution and imaging speed, such as the Vevo LAZR system, which supports real-time 2D and 3D imaging, are available for more NIR-PAI research. All in all, this necessitates a multidisciplinary effort towards optimizing instruments, imaging techniques, and manufacturing standards before clinical application.

In conclusion, our study obtained the histological evidence of QZ formula anti-liver fibrosis in mice, and the correlation analysis results suggest that NIR-PAI kinetic parameters of ICG (T_{max} and $T_{1/2}$) may contribute to non-invasive detection and pharmacodynamic evaluation of LF.

5. Conclusion

In our study, we demonstrated the histological effectiveness of the QZ formula in anti-liver fibrosis, particularly in reducing the deposition

Table 1
General Characteristics of the Different Intervention Mouse Groups.

Variable	Control (n=6)	Model (n=6)	Positive (n=6)	QZ-L (n=6)	QZ-M (n=6)	QZ-H (n=6)	*P* value
Body weight(g)	24.98±1.90	24.26±1.64	24.81±1.90	24.70±1.88	24.83±1.74	24.94±2.47	=0.924
US gray scale ratio (UGSR)	1.0±0.25	1.45±0.17*P<0.0001	1.37±0.11†P=0.8533	1.14 ±0.09†P=0.0005‡P=0.0114	1.10 ±0.10†P<0.0001‡P=0.0020	1.17 ±0.08†P=0.0016‡P=0.0316	<0.05
Diameters of hepatic portal vein, diameters(mm)	1.085±0.103	1.27±0.46	1.17±0.35	0.77±0.20	1.20±0.09	1.27±0.23	=0.0635
Histopathologic staining, Sirius red(%)	0.61±0.4	2.92±0.66*P<0.0001	1.75±0.45†P=0.0017	1.44±0.65†P<0.0001	1.37±0.24†P<0.0001	1.70±0.51†P=0.0016	<0.05
Histopathologic staining, MMP−2(%)	54.38±4.85	31.28±8.41*P=0.0087	62.51±5.83†P=0.0003	60.14±3.52†P=0.0005	61.22±3.46†P=0.0004	52.22±5.06†P=0.0079	<0.05
Histopathologic staining, CD31(%)	29.54±2.97	70.48±3.48*P=0.0008	51.15±7.44†P=0.1528	62.92±12.00†P=0.9477	55.77±1.47†P=0.0409	45.23±4.29†P=0.0109	<0.05
Histopathologic staining, Col−1(%)	84.79±4.47	119.78±16.40*P=0.0254	98.90 ±12.09†P=0.1881	91.88±1.67†P=0.0495	100.54±7.88†P=0.2494	101.49±7.80†P=0.2937	<0.05
Serology content, ALT(IU/L)	25.67±2.42	55.6±19.59*P=0.0001	33.6±4.67†P=0.0086	36.6±6.27†P=0.0294	34±6.16†P=0.0101	31.6±4.61†P=0.0036	<0.05
Serology content, AST(IU/L)	96.66±8.44	145±23.98*P=0.0002	102.2±13.4†P=0.0018	100.8±12.21†P=0.0013	116.6±9.83†P=0.0637	114.4±18.33†P=0.0386	<0.05
Serology content, HA(ng/ml)	422.63±86.19	1285.21 ±479.66*P<0.0001	498.60 ±82.50†P=0.0003	440.10±37.11†P=0.0001	601.435±108.39†P=0.0017	562.41±301.07†P=0.0009	<0.05
Serology content, LN(ng/ml)	26.44±6.04	36.79±4.00*P=0.0149	23.04±4.25†P=0.0008	24.47±4.34†P=0.0043	26.00±5.14†P=0.0151	28.71±4.13†P=0.1118	<0.05
Serology content, Col-IV(ng/ml)	13.12±2.02	35.20±15.83*P=0.0024	11.16±3.55†P=0.0015	12.78±2.23†P=0.0032	16.94±8.01†P=0.0214	18.09±9.88†P=0.0352	<0.05
Serology content, PCIII(ng/ml)	36.25±6.26	63.48±13.94*P=0.0005	44.92±9.67†P=0.0354	39.93±8.68†P=0.0045	36.53±9.51†P=0.0010	31.15±3.23†P<0.0001	<0.05
*T*max (sec)	28±7.93	41±9.67*P<0.0001	30.84±7.67†P=0.0006	30.5±6.49†P=0.0002	33.4±8.99†P=0.0288	30.3±9.14†P=0.0004	<0.001
T1/2 (sec)	304.5±7.65	316.5±8.80 *P<0.0001	307±7.36†P=0.0009	307±6.78†P=0.0007	309.5±7.65†P=0.0349	307.5±7.65†P=0.0021	<0.001

Data are mean ± standard deviation. Abbreviation: ALT = alanine aminotransferase, AST = aspartate aminotransferase, MMP-2=matrix metalloproteinase-2, CD31=cluster of differentiation 31, Col-I=type I collagen protein, HA=hyaluronic acid, LN=laminin, PCIII=type III procollagen, Col-IV=type IV collagen protein. $T_{1/2}$ = half-life, *T*max = maximum peak time. * *P* versus control group. † *P* versus model group. ‡ *P* versus positive group.

of collagen fibers. NIR-PAI combined with ICG is a non-invasive, real-time, and quantitative evaluation tool for plotting liver kinetic parameters. Correlation analysis showed that the PAI kinetic parameters of ICG (T_{max}, $T_{1/2}$) were highly correlated with the histopathology and serology contents in the mice liver, suggesting that NIR-PAI can serve as a non-invasive tool for LF diagnosis and pharmacodynamic evaluation. Table 1

Glossary

Gastroenterology and Hepatology.

Funding

This research was funded by Scientific Research Foundation for New recruits China Academy of Chinese Medical Sciences (No. ZZ16-XRZ-025); Young Elite Scientists Sponsorship Program by CAST (No. 2023QNRC001); Scientific and technological innovation project of China Academy of Chinese Medical Sciences, (No. CI2021A00801 & CI2021A00802); High Level Chinese Medical Hospital Promotion Project (No. HLCMHPP2023086); Sanming Proiectof Medicine in Shenzhen (No. SZZYSM202311014).

CRediT authorship contribution statement

Wen-Liang Lv: Supervision. **Dong Han:** Supervision. **Ning Wang:** Data curation. **Quan-Mei Sun:** Methodology. **Lan-Yu Chen:** Writing – review & editing. **Qing-Juan Wu:** Writing – original draft.

Conflict of interest

All authors have read and agreed to the published version of the manuscript. All the authors declare no conflict of interest.

Declaration of Competing Interest

The authors declare that they have no known competing financial interests or personal relationships that could have appeared to influence the work reported in this paper.

Data Availability

Data will be made available on request.

References

[1] T.A. Wynn, T.R. Ramalingam, Mechanisms of fibrosis: therapeutic translation for fibrotic disease, Nat. Med 18 (2012) 1028–1040.

[2] V. Hernandez-Gea, S.L. Friedman, Pathogenesis of liver fibrosis, Annu Rev. Pathol. 6 (2011) 425–456.

[3] Y.A. Lee, M.C. Wallace, S.L. Friedman, Pathobiology of liver fibrosis: a translational success story, Gut 64 (2015) 830–841.

[4] F. Heymann, F. Tacke, Immunology in the liver–from homeostasis to disease, Nat. Rev. Gastroenterol. Hepatol. 13 (2016) 88–110.

[5] Y. Jiang, F. Hu, M. Li, Q. Li, Tanshinone IIA ameliorates the development of dermal fibrosis in systemic sclerosis, Clin. Exp. Pharm. Physiol. 51 (2024) e13834.

[6] J.Y. Zeng, Y. Wang, F.Y. Hong, M. Miao, Y.Y. Jiang, Z.X. Qiao, Y.T. Wang, et al., Tanshinone IIA is superior to paricalcitol in ameliorating tubulointerstitial fibrosis through regulation of VDR/Wnt/β-catenin pathway in rats with diabetic nephropathy, Naunyn Schmiede Arch. Pharm. (2023).

[7] L. Dan, Y. Hao, H. Song, T. Wang, J. Li, X. He, Y. Su, Efficacy and potential mechanisms of the main active ingredients of Astragalus mongholicus in animal models of liver fibrosis: a systematic review and meta-analysis, J. Ethnopharmacol. 319 (2024) 117198.

[8] X. Niu, Y. Meng, J. Cui, R. Li, X. Ding, B. Niu, G. Chang, et al., Hepatic stellate cell- and liver microbiome-specific delivery system for Dihydrotanshinone I to ameliorate liver fibrosis, ACS Nano 17 (2023) 23608–23625.

[9] N.L. Yao, S.N. Liu, H.B. Yin, Z.S. Chang, Y.N. Bai, W.M. Liu, R.P. Xu, et al., Clinical effect of Qizhu formula on chronic hepatitis B liver fibrosis, 3rd Int. Congr. Tradit. Med. (2004) 05.

[10] X. Wang, J.C. Bamber, R. Esquivel-Sirvent, J. Ormachea, P.S. Sidhu, K. E. Thomenius, S., Jr Schoen, et al., Ultrasonic sound speed estimation for liver fat

quantification: a review by the AIUM-RSNA QIBA pulse-echo quantitative ultrasound initiative, Ultrasound Med. Biol. 49 (2023) 2327–2335.
[11] R.G. Barr, G. Ferraioli, M.L. Palmeri, Z.D. Goodman, G. Garcia-Tsao, J. Rubin, B. Garra, et al., Elastography assessment of liver fibrosis: society of radiologists in ultrasound consensus conference statement, Radiology 276 (2015) 845–861.
[12] M. Zerunian, B. Masci, D. Caruso, F. Pucciarelli, M. Polici, S. Nardacci, D. De Santis, et al., Liver magnetic resonance elastography: focus on methodology, technique, and feasibility, Diagn. (Basel) 14 (2024).
[13] A. Duarte-Rojo, K. Patel, D.C. Rockey, Noninvasive assessment of liver fibrosis and portal hypertension, Curr. Opin. Gastroenterol. 40 (2024) 148–155.
[14] J.X. Liang, J. Ampuero, H. Niu, K. Imajo, M. Noureddin, J. Behari, D.H. Lee, et al., An individual patient data meta-analysis to determine cut-offs for and confounders of NAFLD-fibrosis staging with magnetic resonance elastography, J. Hepatol. 79 (2023) 592–604.
[15] M. Pons, S. Augustin, B. Scheiner, M. Guillaume, M. Rosselli, S.G. Rodrigues, H. Stefanescu, et al., Noninvasive diagnosis of portal hypertension in patients with compensated advanced chronic liver disease, Am. J. Gastroenterol. 116 (2021) 723–732.
[16] Y. Chen, S. Spinelli, Z. Gu, Red/NIR/SWIR multi-band persistent probe chargeable by general lighting sources for long-term,high-contrast visible/NIR-I/NIR-II multi-window bioimaging, Chem. Eng. J. (2022) 446P445.
[17] H. Liu, M. Wang, F. Ji, Y. Jiang, M. Yang, Mini review of photoacoustic clinical imaging: a noninvasive tool for disease diagnosis and treatment evaluation, J. Biomed. Opt. 29 (2024) S11522.
[18] Muraleedharan S., Tripathy K.: Indocyanine Green (I.C.G.) Angiography. In: StatPearls. Treasure Island (FL) with ineligible companies. Disclosure: Koushik Tripathy declares no relevant financial relationships with ineligible companies.: StatPearls Publishing Copyright © 2024, StatPearls Publishing LLC., 2024.
[19] S. Singh, G. Giammanco, C.H. Hu, J. Bush, L.S. Cordova, D.J. Lawrence, J.L. Moran, et al., Size-tunable ICG-based contrast agent platform for targeted near-infrared photoacoustic imaging, Photoacoustics 29 (2023) 100437.
[20] J. Lv, Y. Xu, L. Xu, L. Nie, Quantitative functional evaluation of liver fibrosis in mice with dynamic contrast-enhanced photoacoustic imaging, Radiology 300 (2021) 89–97.
[21] Z. Han, N. Feng, Y. Lu, M. Li, P. Wei, J. Yao, Q. Zhu, et al., A control study on the value of the ultrasound grayscale ratio for the differential diagnosis of thyroid micropapillary carcinoma and micronodular goiter in two medical centers, Front Oncol. 10 (2020) 625238.
[22] N. Feng, P. Wei, X. Kong, J. Xu, J. Yao, F. Cheng, D. Ou, et al., The value of ultrasound grayscale ratio in the diagnosis of papillary thyroid microcarcinomas and benign micronodules in patients with Hashimoto's thyroiditis: a two-center controlled study, Front Endocrinol. (Lausanne) 13 (2022) 949847.
[23] S. Saito, Y. Moriyama, S. Kobayashi, R. Ogihara, D. Koto, A. Kitamura, T. Matsushita, et al., Assessment of liver function in thioacetamide-induced rat acute liver injury using an empirical mathematical model and dynamic contrast-enhanced MRI with Gd-EOB-DTPA, J. Magn. Reson Imaging 36 (2012) 1483–1489.
[24] U. Sabir, H.M. Gu, D.W. Zhang, Extracellular matrix turnover: phytochemicals target and modulate the dual role of matrix metalloproteinases (MMPs) in liver fibrosis, Phytother. Res 37 (2023) 4932–4962.
[25] T. Liu, L. Xu, C. Wang, K. Chen, Y. Xia, J. Li, S. Li, et al., Alleviation of hepatic fibrosis and autophagy via inhibition of transforming growth factor-β1/Smads pathway through shikonin, J. Gastroenterol. Hepatol. 34 (2019) 263–276.
[26] H.J. Kim, S.Y. Kim, S.P. Shin, Y.J. Yang, C.S. Bang, G.H. Baik, D.J. Kim, et al., Immunological measurement of aspartate/alanine aminotransferase in predicting liver fibrosis and inflammation, Korean J. Intern Med 35 (2020) 320–330.
[27] S.H. Moosavy, E. Eftekhar, P. Davoodian, A. Nejatizadeh, M. Shadman, S. Zare, M. A. Nazarnezhad, AST/ALT ratio, APRI, and FIB-4 compared to FibroScan for the assessment of liver fibrosis in patients with chronic hepatitis B in Bandar Abbas, Hormozgan, Iran, BMC Gastroenterol. 23 (2023) 145.
[28] S.K. Venkatesh, M.S. Torbenson, Liver fibrosis quantification, Abdom. Radio. (NY) 47 (2022) 1032–1052.
[29] N. Roehlen, E. Crouchet, T.F. Baumert, Liver fibrosis: mechanistic concepts and therapeutic perspectives, Cells 9 (2020).
[30] O.S. Mohammed, H.G. Attia, B. Mohamed, M.A. Elbaset, H.M. Fayed, Current investigations for liver fibrosis treatment: between repurposing the FDA-approved drugs and the other emerging approaches, J. Pharm. Pharm. Sci. 26 (2023) 11808.
[31] X. Guo, Y. Li, W. Wang, L. Wang, S. Hu, X. Xiao, C. Hu, et al., The construction of preclinical evidence for the treatment of liver fibrosis with quercetin: a systematic review and meta-analysis, Phytother. Res 36 (2022) 3774–3791.
[32] P. Ginès, L. Castera, F. Lammert, I. Graupera, M. Serra-Burriel, A.M. Allen, V. W. Wong, et al., Population screening for liver fibrosis: Toward early diagnosis and intervention for chronic liver diseases, Hepatology 75 (2022) 219–228.
[33] A.J. Sanyal, L. Castera, V.W. Wong, Noninvasive assessment of liver fibrosis in NAFLD, Clin. Gastroenterol. Hepatol. 21 (2023) 2026–2039.
[34] K. Horisberger, F. Rössler, C.E. Oberkofler, D. Raptis, H. Petrowsky, P.A. Clavien, The value of intraoperative dynamic liver function test ICG in predicting postoperative complications in patients undergoing staged hepatectomy: a pilot study, Lange Arch. Surg. 408 (2023) 264.
[35] M. Capozza, F. Blasi, G. Valbusa, P. Oliva, C. Cabella, F. Buonsanti, A. Cordaro, et al., Photoacoustic imaging of integrin-overexpressing tumors using a novel ICG-based contrast agent in mice, Photoacoustics 11 (2018) 36–45.
[36] Q. Wu, Q. Sun, Q. Zhang, N. Wang, W. Lv, D. Han, Extracellular matrix stiffness-induced mechanotransduction of capillarized liver sinusoidal endothelial cells, Pharm. (Basel) 17 (2024).
[37] T. Qiu, J. Yang, C. Peng, H. Xiang, L. Huang, W. Ling, Y. Luo, Diagnosis of liver fibrosis and liver function reserve through non-invasive multispectral photoacoustic imaging, Photoacoustics 33 (2023) 100562.
[38] X. Zhao, G. Zhang, J. Chen, Z. Li, Y. Shi, G. Li, C. Zhai, et al., A rationally designed nuclei-targeting FAPI 04-based molecular probe with enhanced tumor uptake for PET/CT and fluorescence imaging, Eur. J. Nucl. Med Mol. Imaging 51 (2024) 1593–1604.
[39] T. Sun, J. Lv, X. Zhao, W. Li, Z. Zhang, L. Nie, In vivo liver function reserve assessments in alcoholic liver disease by scalable photoacoustic imaging, Photoacoustics 34 (2023) 100569.
[40] G. Huang, J. Lv, Y. He, J. Yang, L. Zeng, L. Nie, In vivo quantitative photoacoustic evaluation of the liver and kidney pathology in tyrosinemia, Photoacoustics 28 (2022) 100410.

Wen-Liang Lv Pro has devoted 90 percent of his practice to liver diseases research for the last forty years both in clinic and laboratory studies. He has extensive experience in viral liver disease, liver fibrosis, cirrhosis and nonalcoholic fatty liver disease. He has previously published several academic papers in the field of liver disease journals.